FASE FRONTIERS OF AGRICULTURAL SCIENCE AND ENGINEERING

Engineering Transactions of CAE

RESEARCH ARTICLE

2026 / Volume 13 / Issue 3 / 25662

Time-varying dynamic modeling and trajectory tracking control for variable-load unmanned aerial vehicle

Xin ZHANG, Shuting XU (✉), Wenjie CHANG, Feng KANG

School of Technology, Beijing Forestry University, Beijing 100083, China.

KEYWORDS

Sliding mode control, tracking control, UAV, variable load

HIGHLIGHTS

- Establishes a time-varying multibody dynamic model for variable-load UAVs, accounting for real-time changes in mass and moment of inertia.
- Designs a robust trajectory tracking control strategy resisting disturbances from load variations and external factors.
- Validates efficacy for agricultural operations, providing experimental support for practical variable-load scenarios.

Received May 26, 2025;
Accepted September 9, 2025.

Correspondence: xushuting@bjfu.edu.cn

GRAPHICAL ABSTRACT

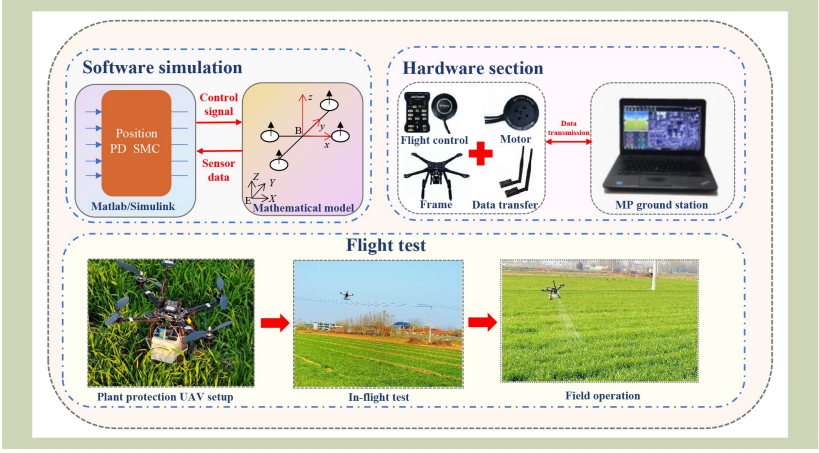

ABSTRACT

The dynamic variation issues of variable-load unmanned aerial vehicle (UAV) used in agricultural plant protection activities was addressed by a disturbance-resistant control system based on PD (proportional-derivative) sliding mode control. First, a time-varying dynamic model was developed by analyzing the variations in mass, center of gravity and moment of inertia across time. Then a trajectory tracking control approach based on PD sliding mode control was designed to develop an inner-loop attitude controller and an outer-loop trajectory controller to accomplish precise and closely coupled trajectory tracking. Numerical simulations were conducted to verify the trajectory tracking performance, demonstrating accurate tracking of the desired trajectory with standard deviations of 0.0507, 0.1613 and 0.0002 m in the horizontal, lateral and vertical directions, respectively. In terms of attitude control, the system exhibited favorable performance on the roll, pitch and yaw axes, with small transient errors and rapid convergence. Flight experiments further demonstrated that the UAV accurately followed the specified path, and errors in both straight and twisting segments satisfied control criteria. This control system ensured efficient and steady trajectory tracking, offering

theoretical and application references for intelligent and precise agricultural plant protection activities.

1 Introduction

The variable-load unmanned aerial vehicle (UAV), as an essential component of smart agriculture, is particularly useful for the prevention and control of agricultural pests and diseases because of their straightforward design, adaptability in terms of mobility and ease of use[1]. These UAVs operate on a rotorcraft platform and have specific pesticide spraying equipment, which allows them to operate in a range of agricultural settings and gave suitable environmental adaptability. Variable-load UAVs have been used extensively in agriculture and have emerged as a key intelligent tool in the pesticide spraying process because of their high operating speed, less risk of chemical drift and improved crop coverage[2]. Despite their remarkable success in real-world applications, UAVs provide control systems with previously unconsidered arising from their intricate operating environments and mission requirements. In particular, the pesticide liquid gradually diminishes over time during spraying operations, causing concurrent temporal changes in the overall mass and moment of inertia of the UAV. Although these modifications occur smoothly, they add time-varying dynamics to the UAV system, which raises the modeling requirements for precise trajectory tracking control and attitude response. Current research in UAV dynamics and control predominantly focuses on modeling frameworks under constant-mass assumptions[3], while studies on variable-load systems mainly concentrate on solid suspension systems[4,5] and abrupt mass changes. Although these methods have made strides in resolving abrupt structural changes, they typically ignore the ongoing dynamic changes brought on by the slow loss of liquid payloads during processes like agricultural spraying. This work systematically models the effects of liquid loss on the center of mass, inertia distribution and flight response of the UAV by explicitly introducing time-varying functions for both mass and moment of inertia in order to address this realistic practical case. A new approach to modeling and controlling variable-mass UAVs in agricultural missions is thus provided by the establishment of a dynamic model with parameter variation and the selection of a trajectory tracking controller physically compatible with this time-evolving behavior.

In the research on UAV suspension systems, Yi et al.[6] investigated the coupling problem between the aircraft and the suspended load, applying the Newton-Euler method to analyze the system modeling of the load swinging effect. Qian & Liu[7] developed the suspended load dynamic models within a two-dimensional plane framework. Tran et al.[8] developed a nonlinear six-degrees-of-freedom dynamic model for quadrotor UAVs. In the research of UAV mass control, Pounds et al[9] performed dynamic modeling for the aerial refueling phase of aircraft. System stability problems during the continuous airlift process of the aircraft were investigated by Xu[10]. The studies above mostly concentrate on simulating the suspension and mass control of large aircraft. The variable-load modeling and control of small rotary-wing UAV require further research.

The UAV control for agricultural plant protection mainly includes proportional-integral-derivative (PID) control algorithm[11–15], linear quadratic regulator (LQR) control algorithm[16–19], active disturbance rejection control (ADRC) algorithm[20–23], adaptive control algorithm and sliding mode control (SMC) algorithm[24–27], and others. The PID algorithm is easy to implement and relatively mature, but parameter tuning is challenging, and the system robustness is relatively weak[28]. LQR control algorithm is a linearized method, making its effectiveness in nonlinear UAV control limited[29]. ADRC algorithm has suitable disturbance-rejection capability, but coordinating multiple adjustable parameters is difficult, and it has poor real-time performance[30]. Adaptive control handles parameter changes and variable loads, making it suitable for time-varying trajectory control of UAVs. However, it is complex, hard to tune, demands high computation, and may degrade under strong disturbances[31–33]. The SMC algorithm offers strong robustness and effectively suppresses parameter uncertainties, making it suitable for attitude and pose control of variable payload multirotor UAVs for agricultural plant protection. Hence, it is essential to investigate how to design a robust, disturbance-rejecting controller to ensure the stable flight of variable-load UAVs.

This paper develops a time-varying dynamic model for variable-load UAV and a disturbance-rejection control system based on PD (proportional-derivative) sliding mode control. The specific contributions include the following. (1) Rigid-body dynamics and CFD-based estimation are combined to create a time-varying dynamic model. This model treats the UAV frame as a rigid body and uses CFD simulations to approximate the variation in mass and inertia of the payload (pesticide tank). This method makes it possible to characterize the dynamic behavior of the UAV more accurately under variable loading conditions and offers a reasonable representation of the impact of payload variation on system dynamics. (2) A disturbance-rejection control strategy is created by combining sliding mode control and PD control. This improves system robustness and guarantees the UAV flight stability and accuracy in challenging situations by enabling a quick response to control errors through the sliding surface design. (3) Actual flight test is introduced to verify the effectiveness of the proposed model and control method.

2 Materials and methods

2.1 Mathematical modeling and problem description of variable-load UAVs

A payload module that can be adjusted, 4-foldable arms, and several motors and rotors make up the variable-load UAVs for agricultural plant protection activities. Based on the needs of the task, the payload module can be classified as either a liquid spraying module or a solid delivery module. Fixing the pesticide tank to the frame and using a pump to pressurize the liquid to the spraying nozzle is the basic idea behind the liquid spraying payload. The stability and mobility of the UAV are greatly impacted by the progressive consumption of pesticide liquid in agricultural plant protection jobs, where the payload mass progressively changes as the pesticide concentration drops.

Owing to this special mechanical structure, the system can be separated into two main modules: the pesticide tank module, whose mass varies gradually, and the constant-mass frame module. Given the disparities in mass distribution, inertia properties and motion dynamics between these modules, multibody dynamic modeling was performed to characterize their dynamic coupling, which effectively captures how payload variations impact UAV performance.

2.1.1 Mathematical modeling of constant-mass frame module

An inertial coordinate system E(X,Y,Z) connected to the center of the Earth and a body-fixed coordinate system B(x,y,z) connected to the center of gravity of the quadrotor are defined as shown in Fig. 1 in order to build the mathematical model for the constant-mass frame module. The roll angle ϕ about the x-axis, pitch angle θ about the y-axis and yaw angle ψ about the z-axis are the definitions of the attitude angles. The rotation matrix R can be used to interconvert these two coordinate systems.

The positional relationship between the two coordinate systems can be written as follows, assuming that the gyroscopic effects of the quadrotor are disregarded:

$$\begin{bmatrix} X \\ Y \\ Z \end{bmatrix} = R \begin{bmatrix} x \\ y \\ z \end{bmatrix} \tag{1}$$

$$R = \begin{pmatrix} C_\theta C_\psi & S_\theta S_\phi C_\psi - S_\psi C_\phi & S_\psi S_\phi + S_\theta C_\phi C_\psi \\ S_\psi C_\theta & C_\phi C_\psi + S_\theta S_\phi S_\psi & S_\theta S_\psi C_\phi - C_\psi S_\phi \\ -S_\theta & S_\phi C_\theta & C_\theta C_\phi \end{pmatrix} \tag{2}$$

where, $[X,Y,Z]^{\mathrm{T}}$ and $[x,y,z]^{\mathrm{T}}$, respectively, are the position coordinates in body-fixed and inertial coordinate systems, S and C are the sine and cosine functions, respectively, and $C_\psi - S_\theta$ is a shortened form of $\cos\psi - \sin\theta$.

According to the relationship between the Euler angles and angular velocities, the following equation can be obtained:

$$\begin{bmatrix} p \\ q \\ r \end{bmatrix} = \begin{bmatrix} 1 & 0 & -S_\theta \\ 0 & C_\phi & S_\theta C_\theta \\ 1 & -S_\phi & C_\phi C_\theta \end{bmatrix} \begin{bmatrix} \dot{\phi} \\ \dot{\theta} \\ \dot{\psi} \end{bmatrix} \tag{3}$$

where, the angular velocity in the body-fixed frame is

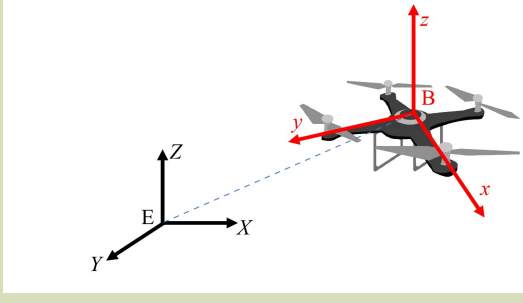

Fig. 1 Definition of coordinate system.

represented by $[p, q, r]^{\mathrm{T}}$ and the corresponding angular velocity in the inertial frame by $[\dot{\phi}, \dot{\theta}, \dot{\psi}]^{\mathrm{T}}$.

Four separate control inputs represent the single force and three moments that the frame experiences during flight: vertical force input U_1, pitch moment input U_2, roll moment input U_3 and yaw moment input U_4. The following matrix equation represents the dynamic model of the frame:

$$\begin{bmatrix} U_1 \\ U_2 \\ U_3 \\ U_4 \end{bmatrix} = \begin{bmatrix} F_1 + F_2 + F_3 + F_4 \\ (F_4 - F_2)l \\ (F_3 - F_1)l \\ D_2 + D_4 - D_1 - D_3 \end{bmatrix} \tag{4}$$

where, l is the distance between the rotor center and the origin of the body-fixed coordinate system, F_i is the lift that each rotor produces and D_i is the response torque that each rotor produces.

Their correlations with rotor speed ω_i are expressed as:

$$T_i = k_t\omega_i^2,\ D_i = k_d\omega_i^2 \tag{5}$$

where, the moment constant is k_d and the thrust constant is k_t. From this equation, the following relationships can be obtained:

$$\begin{bmatrix} U_1 \\ U_2 \\ U_3 \\ U_4 \end{bmatrix} = \begin{bmatrix} k_t \sum_{i=1}^{4} \omega_i^2 \\ k_t(\omega_4^2 - \omega_2^2)l \\ k_t(\omega_3^2 - \omega_1^2)l \\ k_d(\omega_2^2 + \omega_4^2 - \omega_1^2 - \omega_3^2) \end{bmatrix} \tag{6}$$

where, F_x, F_y and F_z are the corresponding components of F_B along the x, y and z axes in the inertial coordinate system, respectively.

With F_B representing the force produced by the rotors in the body-fixed coordinate system is:

$$F_B = \begin{bmatrix} 0 \\ 0 \\ U_1 \end{bmatrix} \tag{7}$$

The relationship between F_B and F_x, F_y and Fz based on the coordinate transformation matrix R is:

$$\begin{bmatrix} F_x \\ F_y \\ F_z \end{bmatrix} = RF_B = U_1 \begin{bmatrix} C_\phi S_\theta C_\psi + S_\phi S_\psi \\ C_\phi S_\theta S_\psi - S_\phi C_\psi \\ C_\phi C_\theta \end{bmatrix} \tag{8}$$

Newton's second law and mechanical analysis yield the dynamic equations of the frame:

$$\begin{cases} \ddot{x} = \dfrac{F_x + K_1\dot{x}}{m} = \dfrac{U_1(C_\phi S_\theta C_\psi + S_\phi S_\psi) + K_1\dot{x}}{m} \\ \ddot{y} = \dfrac{F_y + K_2\dot{y}}{m} = \dfrac{U_1(C_\phi S_\theta S_\psi - S_\phi C_\psi) + K_2\dot{y}}{m} \\ \ddot{z} = \dfrac{F_z + K_3\dot{z} - mg}{m} = \dfrac{U_1 C_\phi C_\theta + K_3\dot{z}}{m} - g \end{cases} \tag{9}$$

where, m is the mass of the UAV frame and K_i is the drag coefficient in linear motion.

The diagonal matrix I can be used to define the inertia matrix of the UAV if its mass and structure are symmetric:

$$I = \begin{bmatrix} I_x & & \\ & I_y & \\ & & I_z \end{bmatrix} \tag{10}$$

The total moment M operating on the quadrotor can be explained as follows using Euler's equation:

$$M = I\begin{bmatrix} \dot{p} \\ \dot{q} \\ \dot{r} \end{bmatrix} + \begin{bmatrix} p \\ q \\ r \end{bmatrix} \times I \begin{bmatrix} p \\ q \\ r \end{bmatrix} \tag{11}$$

By calculation, this can be simplified to the following form:

$$\begin{cases} \dot{p} = \dfrac{LU_2 + (I_y - I_z)qr}{I_x} \\ \dot{q} = \dfrac{LU_3 + (I_z - I_x)pr}{I_y} \\ \dot{r} = \dfrac{LU_4 + (I_x - I_y)pq}{I_z} \end{cases} \tag{12}$$

The final mathematical model of the frame is:

$$\begin{cases} \ddot{x} = \dfrac{F_x + K_1\dot{x}}{m} = \dfrac{U_1(C_\phi S_\theta C_\psi + S_\psi S_\theta) + K_1\dot{x}}{m} \\ \ddot{y} = \dfrac{F_y + K_2\dot{y}}{m} = \dfrac{U_1(C_\phi S_\theta S_\psi - S_\psi C_\theta) + K_2\dot{y}}{m} \\ \ddot{z} = \dfrac{F_z + K_3\dot{z} - mg}{m} = \dfrac{U_1 C_\phi C_\theta + K_3\dot{z}}{m} - g \\ \dot{p} = \dfrac{LU_2 + (I_y - I_z)qr}{I_x} \\ \dot{q} = \dfrac{LU_3 + (I_z - I_x)pr}{I_y} \\ \dot{r} = \dfrac{LU_4 + (I_x - I_y)pq}{I_z} \end{cases} \tag{13}$$

2.1.2 Mathematical modeling of the pesticide tank module

The outflow of liquid from the pesticide tank causes notable variations in the instantaneous mass attributes of the UAV, such as overall mass and moment of inertia, during the agricultural plant protection operations of a variable-load UAV with a quadrotor design. The accuracy and stability of the light control system may suffer as a result of these modifications. This study makes the following assumptions to guarantee both computational viability and physical plausibility.

Assumption 1: the pesticide tank is a rectangular cuboid, symmetric about the x and y axes, and its center is aligned along the z-axis of the body-fixed coordinate system.

Assumption 2: the pesticide tank has damping grids put inside, which creates a comparatively stable liquid surface while the spraying is going on. Therefore, when simulating the variable-load UAV during agricultural plant protection missions, liquid sloshing effects are disregarded.

Assumption 3: the thickness of the pesticide tank walls is omitted, and only the contribution of the interior liquid to the overall mass and moment of inertia is considered.

The fluid volume (FV) multiphase flow model, which tracks the interface between phases, is used in this work to numerically evaluate the variation in the moment of inertia brought on by liquid leakage during spraying operations. The study focuses on the gas-liquid two-phase flow inside the pesticide tank. A time-varying mathematical model of a quadrotor variable-load UAV is developed based on these simulations. The FV approach provides a volume fraction function, with φ_q the fraction of liquid within each computational cell, so permitting the tracking of the dynamic evolution of the free surface without explicitly following individual fluid particles on the liquid interface.

The pesticide is represented in the simulation as water since its physical characteristics, such as density and viscosity, are quite comparable to those of liquid water. The computational fluid dynamics (CFD) program ANSYS Fluent is used to do a three-dimensional transient simulation of the liquid motion inside the pesticide tank. The computational domain is separated into two regions: the external flow field, which represents the area, where the liquid is sprayed into the surrounding space and the internal flow field, which represents the liquid inside the pesticide tank. The physical model is built in SolidWorks at a 1:1 scale. For numerical analysis, the model is integrated into the simulation program after being exported in STL format.

The boundary condition settings are: (1) the top of the pesticide tank is an air region and water is the working fluid during the simulation; (2) a clear gas-liquid interface is maintained during the spraying and drainage process, with no interpenetration between the two phases; (3) the FV method is used for transient multiphase flow calculation; (4) the standard k-ε turbulence model is used to account for the turbulent characteristics of localized flow during spraying; (5) the spraying velocity is set to 0.43 $m \cdot s^{-1}$, for a total of 100 s; and (6) the tank is initially filled to 100% of its capacity with liquid.

A user defined function is created to move through each computational cell in the simulation domain in order to determine the dynamic variation of the liquid center of mass and moment of inertia. The volume fraction indicates if liquid is present in each cell, and the liquid mass distribution, center of mass and moment of inertia are then computed in relation to a coordinate system set up in the center of the bottom surface of the tank. Figures 2 and 3 show the liquid phase distribution diagrams and velocity contour maps at four time steps.

Figure 4 show the time evolution of the moments of inertia of the liquid about the primary axis during the spraying operation. The moments of inertia in all three directions steadily drop with time and approach zero at the end of the spraying procedure (100 s).

To investigate the trends of variation in the moments of inertia over time, a curve fitting analysis was performed. The data was subjected to linear models, quadratic polynomial models and exponential decay models in the I_{xx}, I_{yy} and I_{zz} directions, respectively. After comparing fitting ability of each model, the model that best represented the time-dependent variation of the moments of inertia in each direction was chosen based on its goodness-of-fit (R^2 and adjusted R^2) and error metrics (MSE and RMSE). Tables 1–3 summarize the fitted results.

The time history of the entire liquid mass is shown in Fig. 5. A steady and continuous spraying process with a constant discharge rate is revealed by the linear and uniform drop of the mass from an initial value of about 1.5 kg to zero at about 100 s.

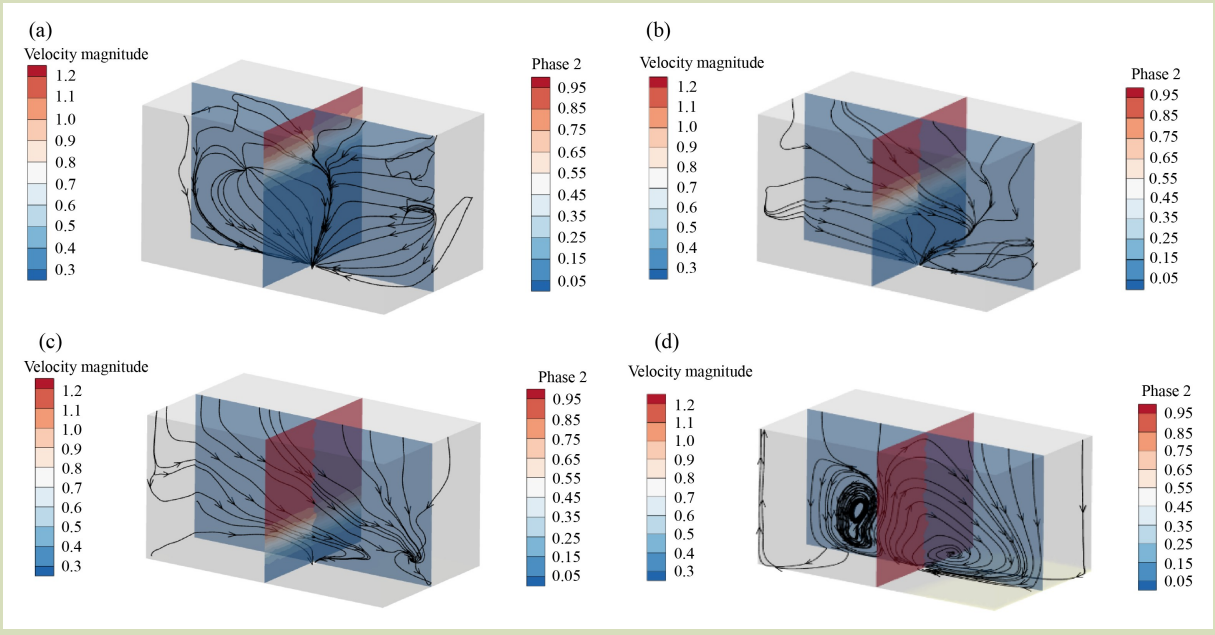

Fig. 2 Velocity contour plots at four time steps: (a) 25 s, (b) 50 s, (c) 75 s, and (d) 100 s.

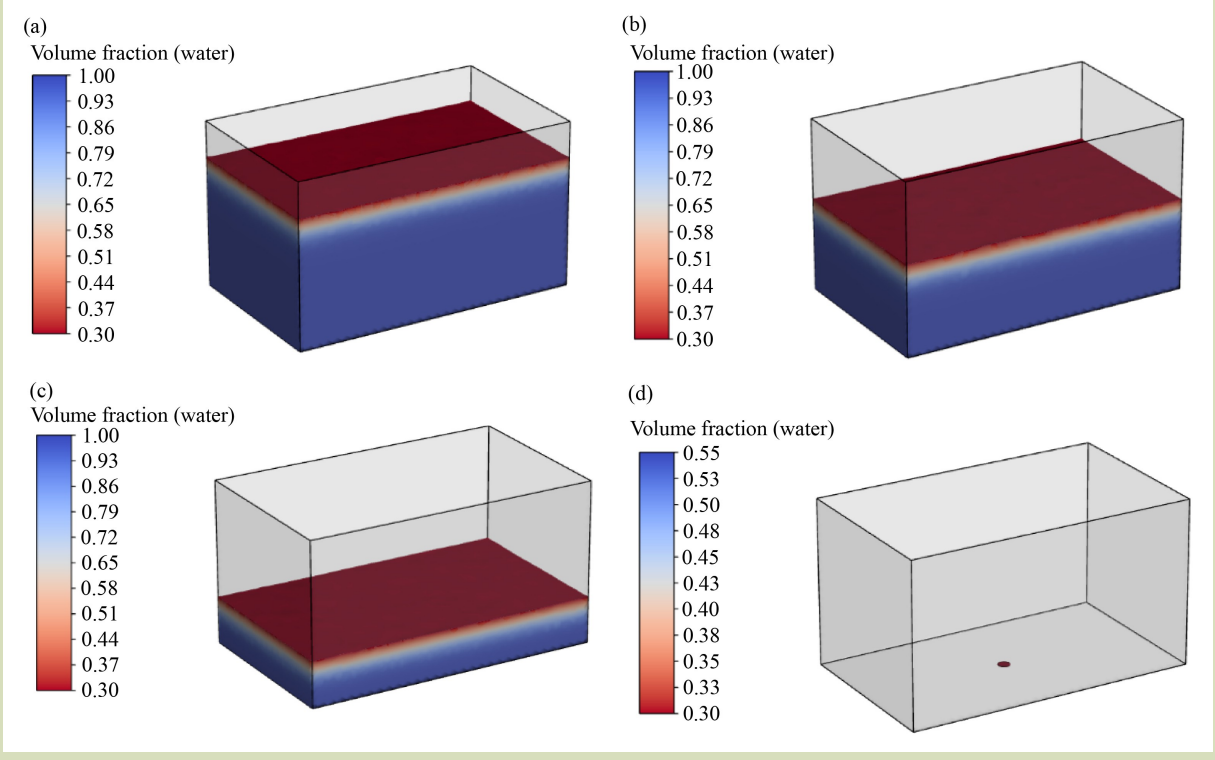

Fig. 3 Water phase diagrams at four time steps: (a) 25 s, (b) 50 s, (c) 75 s, and (d) 100 s.

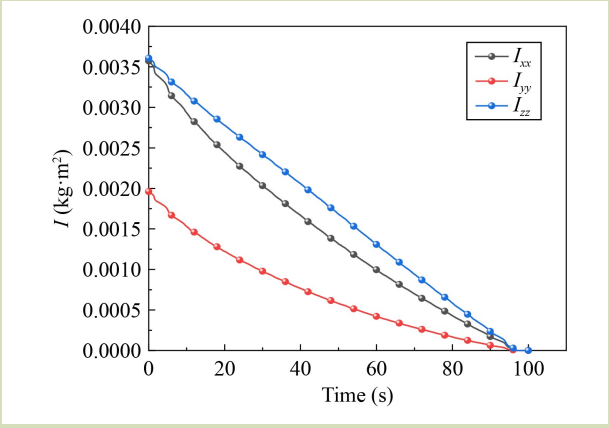

Fig. 4 Variation of moment of inertia over time. I_{xx}, I_{yy} and I_{zz} represent the moments of inertia about the *x*-axis, *y*-axis, and *z*- axis, respectively.

Table 4 provides a summary of the mass of the tank as a function of time.

Figure 6 shows the liquid center of the time-varying trajectories of the mass in the *x*-, *y*- and *z*-directions. A homogeneous discharge of the liquid along the vertical axis is shown by the center of the overall linear downward tendency of the mass in the z-direction. There are not many changes in the *x* and *y*-directions, which indicates that the spraying process is stable and symmetric. Numerical disturbances resulting from the depletion of the liquid are probably the origin of the small oscillations seen near the end of the procedure.

2.1.3 Mathematical modeling of variable-load UAVs

The time-varying multibody dynamic model of the variable-load UAV can be obtained as follows using the synopsis of the preceding two sections:

Table 1 Regression model comparison for I_{XX} as a function of time

Model	Fitted function	Rank			
		R^2	Adjusted R^2	MSE	RMSE
Linear	$y = 3.44 \times 10^{-3} - 5.10 \times 10^{-5}x$	0.984	0.984	1.60×10^{-8}	0.000126
Quadratic	$y = 3.44 \times 10^{-3} - 5.11 \times 10^{-5}x + 1.67 \times 10^{-7}x^2$	0.9996	0.999	9.16×10^{-10}	3.03×10^{-5}
Exponential	$y = 0.00553 \times e^{-0.0348x}$	0.800	0.800	0.237	0.487

Table 2 Regression model comparison for I_{YY} as a function of time

Model	Fitted function	Rank			
		R^2	Adjusted R^2	MSE	RMSE
Linear	$y = -3.56 \times 10^{-3} - 3.86 \times 10^{-5}x$	0.957	0.957	1.26×10^{-8}	0.000112
Quadratic	$y = 3.56 \times 10^{-3} - 3.86 \times 10^{-5}x + 1.92 \times 10^{-8}x^2$	0.998	0.998	1.26×10^{-8}	2.45×10^{-5}
Exponential	$y = 0.003002 \times e^{-0.0389x}$	0.839	0.839	0.227	0.476

Table 3 Regression model comparison for I_{ZZ} as a function of time

Model	Fitted function	Rank			
		R^2	Adjusted R^2	MSE	RMSE
Linear	$y = -3.56 \times 10^{-3} - 3.86 \times 10^{-5}x$	0.9997	0.9997	3.36×10^{-10}	1.83×10^{-5}
Quadratic	$y = 3.56 \times 10^{-3} - 3.86 \times 10^{-5}x + 1.92 \times 10^{-8}x^2$	0.9999	0.9999	1.55×10^{-10}	1.24×10^{-5}
Exponential	$y = 0.00593 \times e^{-0.0318x}$	0.748	0.748	0.267	0.517

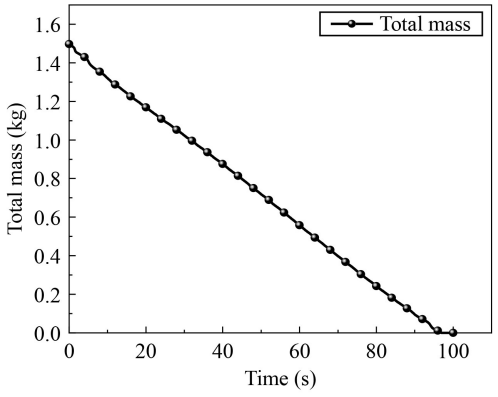

Fig. 5 Variation of mass of the tank over time.

$$\begin{cases} \ddot{x} = \dfrac{U_1(C_\phi S_\theta C_\psi + S_\psi S_\theta) + K_1\dot{x}}{m} \\ \ddot{y} = \dfrac{U_1(C_\phi S_\theta S_\psi - S_\psi C_\theta) + K_2\dot{y}}{m} \\ \ddot{z} = \dfrac{U_1 C_\phi C_\theta + K_3\dot{z}}{m} - g \\ \dot{p} = \dfrac{LU_2 + (I_Y - I_Z)qr}{I_x} \\ \dot{q} = \dfrac{LU_3 + (I_Z - I_X)pr}{I_Y} \\ \dot{r} = \dfrac{LU_4 + (I_X - I_Y)pq}{I_Z} \end{cases} \quad (14)$$

where:

$$\begin{cases} m = 1.48 - 0.0154t + 2.00\times10^{-6}t^2 \\ I_x = I_{x_1} + I_{x_2} \\ I_Y = I_{y_1} + I_{y_2} \\ I_Z = I_{z_1} + I_{z_2} \\ I_{x_1} = 3.44\times10^{-3} - 5.11\times10^{-5}t + 1.67\times10^{-7}t^2 \\ I_{y_1} = 1.86\times10^{-3} - 3.30\times10^{-5}t + 1.47\times10^{-7}t^2 \\ I_{z_1} = 3.56\times10^{-3} - 3.86\times10^{-5}t + 1.92\times10^{-8}t^2 \end{cases} \quad (15)$$

3 Time-varying control system design

The time-varying multibody dynamic model of the variable-load UAV can be obtained using the synopsis of the preceding two sections. As depicted in Fig. 7 (Control system block diagram), this dynamic model serves as the core feedback and simulation basis for the UAV's control system, where key parameters such as real-time load mass and moment of inertia derived from the model are transmitted to the flight controller to optimize control strategies and ensure flight stability.

In the dynamic model, U_2, U_3 and U_4 regulate the flight attitude of the UAV, while U_1 regulates translational motion along the X, Y and Z axes. A cascaded controller with an inner/outer-loop topology is intended to meet the trajectory tracking goals of the variable-load UAV. A PD-based sliding mode controller is used in the attitude control loop to precisely track the reference attitude angles and guarantee attitude stability. To allow for high-precision tracking of the reference trajectory, the position control loop uses a sliding mode controller for the position subsystem. Under constantly changing payload conditions, system stability and trajectory tracking performance are guaranteed by the coordinated operation of the dual-loop control.

3.1 Controller design

U_1 needs to be broken down into three distinct virtual control inputs, U_x, U_y and U_z, which correspond to the control components along the X-, Y- and Z-directions, respectively, because it functions as a composite input for controlling displacement along the X-, Y- and Z-axes, but in real operation, the control demands in these three directions are independent. For each of these virtual control variables, a suitable control algorithm will be created separately. The dynamic model states that these virtual control inputs are:

Table 4 Regression model comparison for mass of the tank as a function of time

Model	Fitted function	Rank			
		R^2	Adjusted R^2	MSE	RMSE
Linear	$y = -1.48 - 0.0153x$	0.9996	0.9996	7.93×10^{-5}	0.00890
Quadratic	$y = 1.48 - 0.0155x + 2.00\times10^{-6}x^2$	0.9996	0.9996	7.80×10^{-5}	0.00883
Exponential	$y = 2.644\times e^{-0.0336x}$	0.659	0.659	0.460	0.678

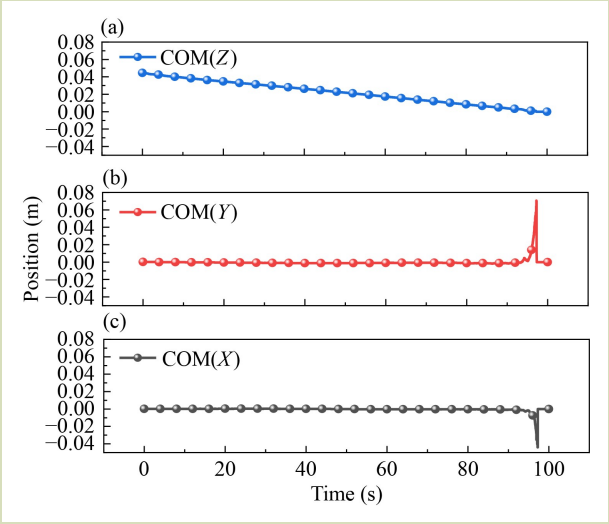

Fig. 6 Variation of the liquid center of mass over time: (a) *x*-direction, (b) *y*-direction and (c) *z*-direction.

$$\begin{cases} U_x = U_1 (C_\phi S_\theta C_\psi + S_\phi S_\psi) \\ U_y = U_1 (C_\phi S_\theta S_\psi - S_\phi C_\psi) \\ U_z = U_1 C_\phi C_\theta \end{cases} \tag{16}$$

Inverse computation can be used to determine the desired roll angle (ϕ_d), the desired pitch angle (θ_d), and the desired yaw angle (ψ_d) based on the dynamic model given above and the input U_1:

$$\begin{cases} U_1 = m\sqrt{u_x^2 + u_y^2 + (u_z + g)^2}, \\ \phi_d = \arcsin\left(\dfrac{m(u_x \sin\psi_d - u_y \cos\psi_d)}{U_1}\right) \\ \theta_d = \arctan\left(\dfrac{m(u_x \cos\psi_d + u_y \sin\psi_d)}{u_z + g}\right) \end{cases} \tag{17}$$

The purpose of the outer control loop is to achieve reference trajectory tracking of the position of the UAV in the *X*-, *Y*- and *Z*-directions. Assuming the reference trajectory is represented as (x_d, y_d and z_d), the position tracking error is:

$$\begin{cases} e_x = x_d - x \\ e_y = y_d - y \\ e_z = z_d - z \end{cases} \tag{18}$$

The derivative yields the following rate of change for the position tracking error:

$$\begin{cases} \dot{e}_x = \dot{x}_d - \dot{x} \\ \dot{e}_y = \dot{y}_d - \dot{y} \\ \dot{e}_z = \dot{z}_d - \dot{z} \end{cases} \tag{19}$$

To guarantee the tracking quick convergence of the error, the sliding surface is described as follows. It is specifically designed to include both proportional and derivative terms, thereby embedding the dynamic response characteristics of a classical PD controller into the sliding mode control framework. This

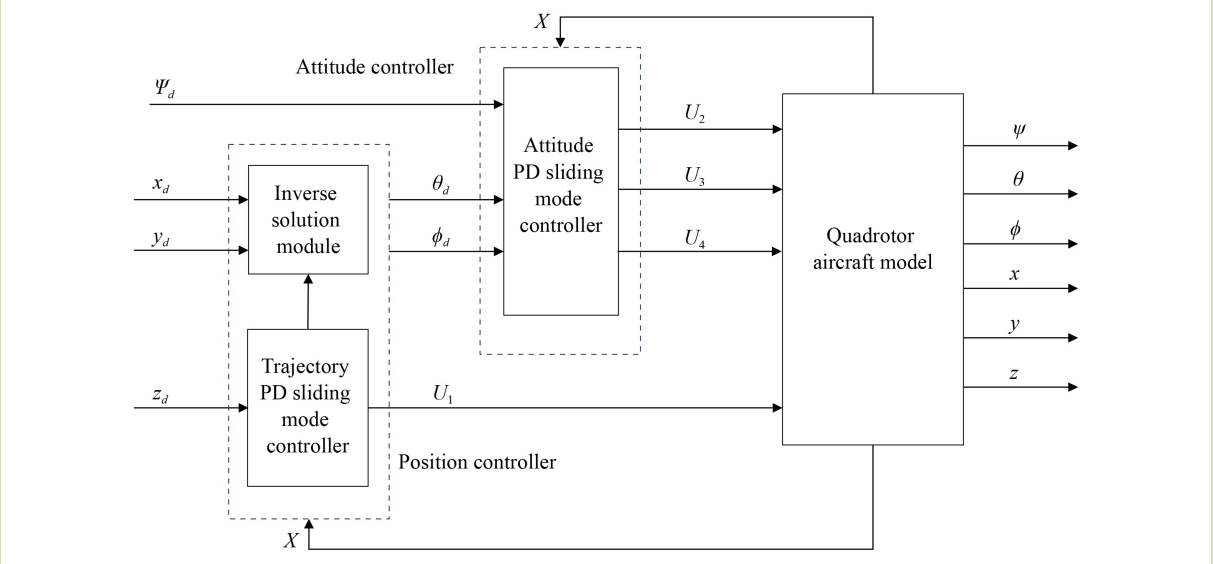

Fig. 7 Control system block diagram.

structure enhances the ability of the system to respond rapidly to tracking errors while retaining the robustness inherent to sliding mode control:

$$s_i = K_{Pi}e_i + K_{Di}\dot{e}_i \tag{20}$$

With $s_i = [s_x, s_y, s_z]$ being the sliding surface, K_{pi}, K_{Di} are the proportional and derivative gain vectors, respectively, and all elements positive. The time derivative of the position sliding surface is:

$$\dot{s}_i = K_{Pi}\dot{e}_i + K_{Di}\ddot{e}_i \tag{21}$$

The sliding mode control law is:

$$\dot{s}_i = -\alpha_i |s_i|^{\beta_i} \operatorname{sgn}(s_i) - k_i s_i \tag{22}$$

where, $\dot{s}_i = [\dot{s}_x, \dot{s}_y, \dot{s}_z]$, $\alpha_i = [\alpha_x, \alpha_y, \alpha_z]$, $\alpha_i > 0$, $\beta_i = [\beta_x, \beta_y, \beta_z]$, $0 \leqslant \beta_i \leqslant 1$, $k_i = [k_x, k_y, k_z]$, $k_i > 0$

To mitigate the chattering phenomenon in the UAV system, the continuous hyperbolic tangent function $\tanh(x)$ is used to replace the discontinuous sign function $\operatorname{sgn}(x)$, thereby reducing sliding mode chattering. The modified sliding mode reaching law is expressed as:

$$\dot{s}_i = -\alpha_i |s_i|^{\beta_i} \tanh(s_i) - k_i s_i \tag{23}$$

where:

$$\tanh(x) = \frac{\sinh(x)}{\cosh(x)} = \frac{e^x - e^{-x}}{e^x + e^{-x}} \tag{24}$$

The final control laws for the three channels are:

$$\begin{cases} u_x = \ddot{x}_d - d_x + (K_{P_x}\dot{e}_x - \dot{s}_x)\dfrac{1}{K_{D_x}} \\ u_y = \ddot{y}_d - d_y + \left(K_{P_y}\dot{e}_y - \dot{s}_y\right)\dfrac{1}{K_{D_y}} \\ u_z = \ddot{z}_d - d_z + g + (K_{P_z}\dot{e}_z - \dot{s}_z)\dfrac{1}{K_{D_z}} \end{cases} \tag{25}$$

Similarly, the control rules for the roll angle (ϕ) channel as U_2, the pitch angle (θ) channel as U_3 and the yaw angle (ψ) channel as U_4 are:

$$\begin{cases} U_2 = \dfrac{I_X}{K_{D_\phi}}\left(K_{P_\phi}\dot{e}_\phi - \dot{s}_\phi\right) + I_X\ddot{\phi}_d - (I_Z - I_Y)\dot{\psi}\dot{\theta} \\ U_3 = \dfrac{I_Y}{K_{D_\theta}}(K_{P_\theta}\dot{e}_\theta - \dot{s}_\theta) + I_Y\ddot{\theta}_d - (I_X - I_Z)\dot{\phi}\dot{\psi} \\ U_4 = \dfrac{I_Z}{K_{D_\psi}}\left(K_{P_\psi}\dot{e}_\psi - \dot{s}_\psi\right) + I_Z\ddot{\psi}_d - (I_Y - I_X)\dot{\theta}\dot{\phi} \end{cases} \tag{26}$$

3.2 Stability analysis

After the controller design is completed, a stability analysis is performed using the Lyapunov criterion. Taking the X-channel as an example, the stability of the control law is verified. The Lyapunov function is chosen as:

$$V_{s_x} = \frac{1}{2}s_x^2 \tag{27}$$

By taking the derivative, the following is obtained:

$$\begin{aligned} \dot{V}_{s_x} &= s_x\dot{s}_x \\ &= s_x(K_{P_x}\dot{e}_x + K_{D_x}\ddot{e}_x)n \\ &= s_x[K_{P_x}\dot{e}_x + K_{D_x}(\ddot{x}_d - \ddot{x})]n \\ &= s_x[K_{P_x}\dot{e}_x + K_{D_x}\ddot{x}_d - K_{D_x}(u_x + d_x)]n \\ &= s_x\left[K_{P_x}\dot{e}_x + K_{D_x}\ddot{x}_d - K_{D_x}\left(\frac{1}{K_{D_x}}(K_{P_x}\dot{e}_x - \dot{s}_x)\right)\right]n \\ &= s_x\left[K_{P_x}\dot{e}_x + K_{D_x}\ddot{x}_d - K_{P_x}\dot{e}_x - \alpha_x|s_x|^{\beta_x}\tanh(s_x) - k_x s_x\right]n \\ &= s_x(-\alpha_x|s_x|\tanh(s_x) - k_x s_x)n \\ &\quad - k_x s_x^2 \leqslant 0 \end{aligned} \tag{28}$$

Therefore, $s_x\dot{s}_x < 0$, the above analysis satisfies the sliding mode stability condition, which holds if and only if $s_x = 0$, $\dot{V}_{x_k} = 0$, The closed-loop system is asymptotically stable, meaning that s_x approaches zero as t approaches infinity.

4 Simulation

The PD sliding mode controller was used in Simulink simulation trials to confirm the viability and efficacy of the controller. To ensure that the simulation model adequately reflects the dynamic characteristics of the real system, the controller design and parameter settings were based on measurement data and computational results from the actual UAV. Table 5 lists the particular parameters of the model along with the values that correspond to them.

During the first 0–10 s, the UAV climbs 4 m along the positive Z-axis to simulate the agricultural plant protection operation of

Table 5 Parameter and unit of variable-load UAVs

Parameter	Value	Unit
m	1.5	kg
I_{x_2}	0.0072	kg·m^2
I_{y_2}	0.0072	kg·m^2
I_{z_2}	0.00102	kg·m^2
l	0.18	m
K	0.012	(N·s)·m^{-1}
g	9.81	m·s^{-2}

a variable-load UAV. From 10 to 100 s, it executes a uniform-speed boustrophedon motion in the *x*-*y* plane with one complete cycle.

It is evident from Figs. 5, 6 and 8 that the system is able to track the trajectory effectively along all three axes (*X*, *Y* and *Z*). In both *X*- and *Y*-directions, as shown in Fig. 8(a,b), the actual path closely resembles the desired trajectory, with only minor deviations at curvature transitions that are promptly corrected by the controller, indicating strong stability and control accuracy. In the *Z*-direction, as depicted in Fig. 8(c), even though the desired trajectory involves a vertical rise from 0 to 4 m over the first 10 s followed by a steady hold at 4 m from 10 to 100 s, the actual trajectory mimics this profile with high fidelity, keeping the error within a tolerable range. Figure 9 further quantifies the trajectory tracking errors.

The system provides adequate trajectory tracking performance in three-dimensional space, as illustrated in Fig. 10. The reference trajectory closely resembles the actual trajectory. Robust control in planar motion is indicated by the small mistakes seen in the *X*- and *Y*-directions. The ability of the system to swiftly correct deviations and return to the reference path at turning points demonstrates its dynamic reaction capabilities. Strong flexibility and steady control are demonstrated by the capacity of the system to track height changes in the *Z*-direction with great precision and consistency. Overall, the system gave dynamic performance in 3D space and dependable control precision.

The system keeps tracking errors within allowable bounds on all three spatial axes, based on the data in Table 6. High precision and consistent control are indicated by the maximum error of 0.177 m, mean error of 0.0004 m, and standard deviation of 0.0507 m along the *X*-axis. With a mean of 0.0281 m and a standard deviation of 0.161 m along the *Y*-axis, the maximum error is 0.927 m, indicating high adaptability to dynamic changes. The mean error and standard deviation are insignificant, and the highest error for the *Z*-axis is under 0.002 m, indicating strong stability and outstanding vertical tracking accuracy.

As illustrated in Fig. 11, the system demonstrates effective control of the roll, pitch and yaw angles. With minor deviations mostly occurring during abrupt attitude changes, the actual trajectories closely match the intended ones. These mistakes are little in scope and are quickly fixed. All things considered, the system meets the requirements for reliable flight control by

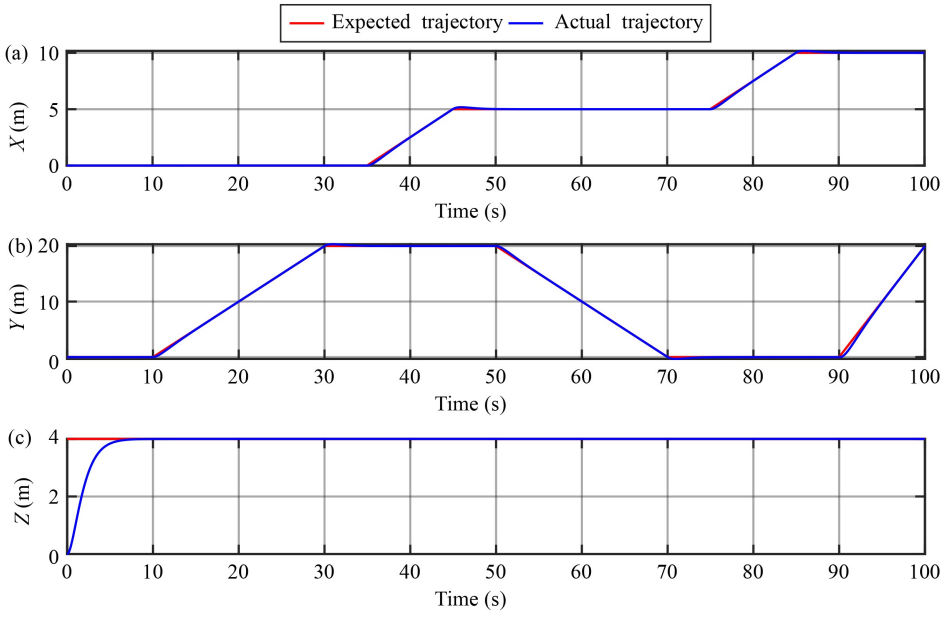

Fig. 8 Simulation results of trajectory tracking: (a) *X*-direction, (b) *Y*-direction, and (c) *Z*-direction.

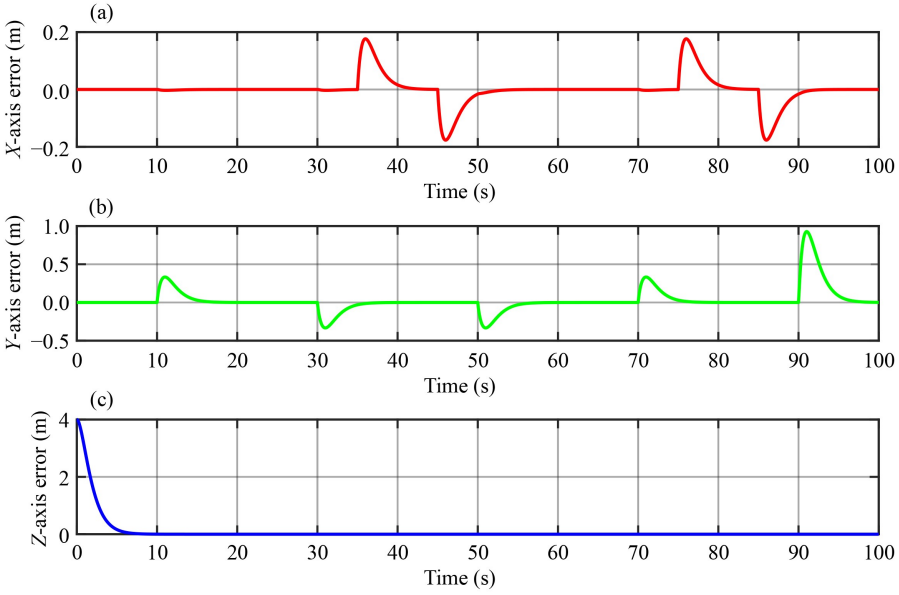

Fig. 9 Simulation results of trajectory tracking error: (a) *X*-axis, (b) *Y*-axis, and (c) *Z*-axis.

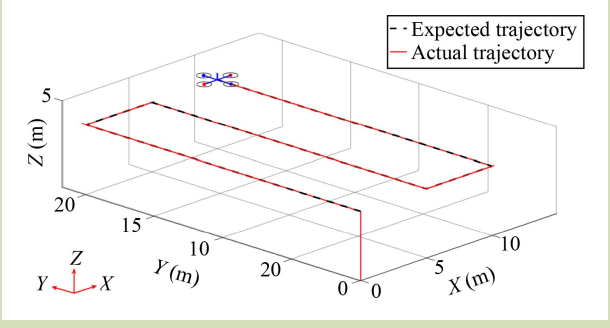

Fig. 10 3D trajectory tracking. Black dashed line, reference trajectory; and red line, actual trajectory.

guaranteeing high precision in attitude control and displaying favorable dynamic response characteristics.

To further verify the advantages of the proposed control method, comparative simulations with PID control and conventional SMC control were conducted. The results (Fig. 12) indicate that: (1) in the *X*- and *Y*-directions, PD sliding mode control tracks the reference trajectory with high accuracy, while PID and SMC exhibit noticeable deviations; (2) in the *Z*-direction, PD sliding mode control achieves the fastest response and the smallest overshoot, demonstrating superior stability compared with the other methods; and (3) overall, PD sliding mode control gave the best performance in terms of accuracy, robustness, and dynamic response for three-dimensional trajectory tracking.

Table 6 Error analysis of trajectory tracking

Coordinate axis	Tracking deviation index (m)		
	Max	Mean	SD
X	0.177	0.0004	0.0507
Y	0.927	0.0281	0.161
Z	0.002	0.00002	0.0002

These results not only confirm the reliability of the proposed method but also clearly demonstrate its superiority over conventional control approaches.

5 Experimental validation

Using a genuine quadrotor UAV, flight tests were performed to confirm the viability of the chosen UAV dynamic model and the time-varying controller. Figure 9 shows the experimental

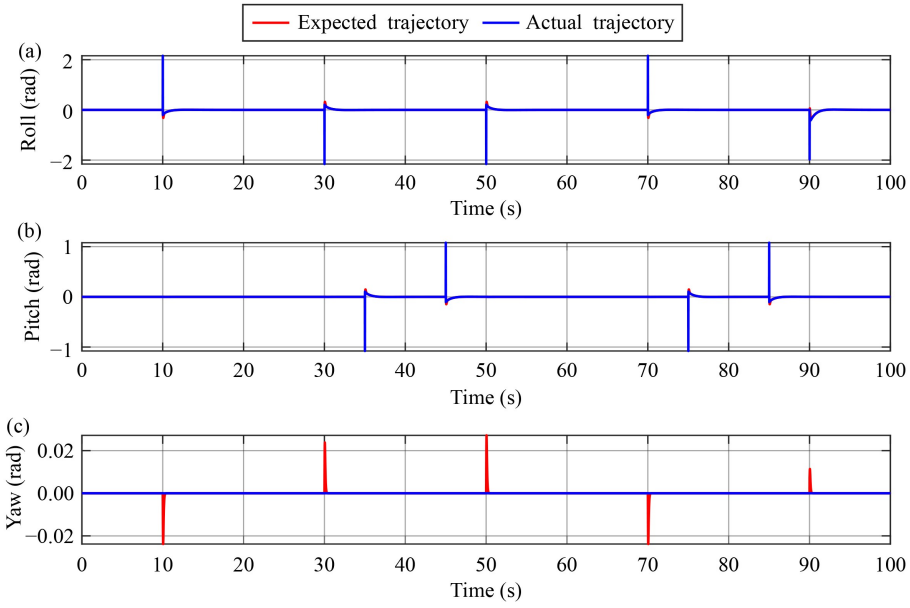

Fig. 11 Results of attitude control: (a) roll angle, (b) pitch angle, and (c) yaw angle.

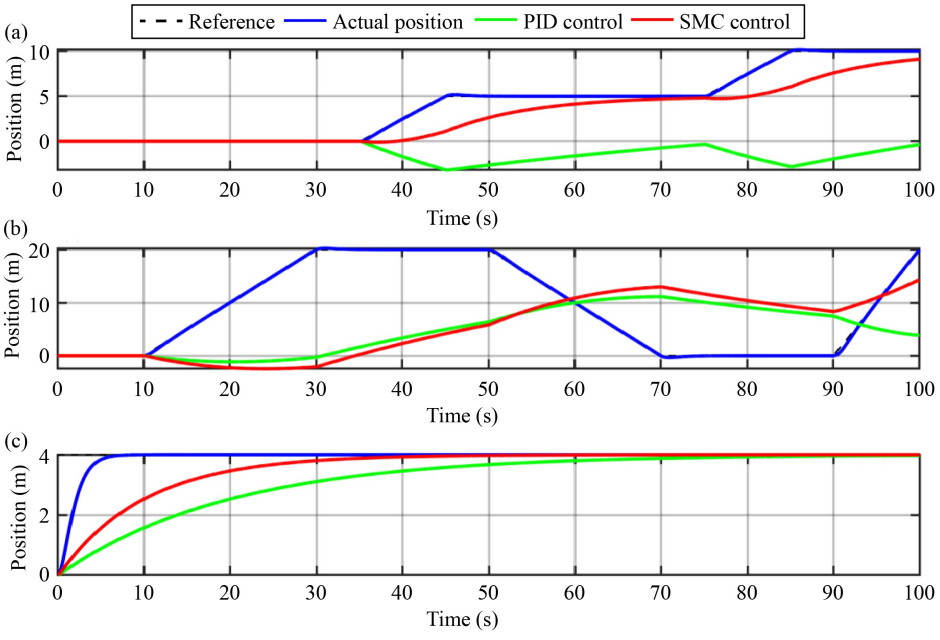

Fig. 12 Comparative results of three-dimensional trajectory tracking under different control methods: *X*-axis, (b) *Y*-axis, and (c) *Z*-axis. Black dashed line, reference trajectory; blue line, actual position with PD sliding mode control; green line, PID control; and red line, SMC control.

configuration. The Pixhawk 2.4.8 flight control system is installed on the UAV. To ensure stable and accurate flight control, precise attitude angle measurements are made using a six-axis measuring unit (MPU6050). Reliable functioning in challenging situations is made possible by the integration of an M8N GPS module, which offers high-precision location. To handle the power needs of the UAV, the propulsion system consists of 3507 motors coupled with Letian 20A electronic speed controllers. Real-time data interchange and reliable communication are maintained by using a PIX 2.4.8 data transmission module. The time-varying controller created in the previous section was used to provide flight control, and the dynamic reaction of the UAV during actual flight closely matches the simulation results. Figure 13 shows the assembly and configuration of a UAV for agricultural plant protection.

The algorithm validation flight test was conducted in Hebei Province. The plants in the testing area were around 15 cm tall and were situated in a level wheat field. The level and broad landscape allowed for accurate replication of real-world field conditions and was ideal for UAV agricultural spraying operations. The UAV flew at a consistent 4 m altitude and a steady pace while carrying a full water tank. During the test, wind conditions were mild and airflow disturbances remained minimal. The overall environment was stable, offering well-bounded conditions that effectively minimized the influence of uncertain factors such as wind on the experimental outcomes.

Flight data were acquired using the Mission Planner ground station. The mission featured a vertical takeoff followed by altitude stabilization at 4 m. After completing the mission, the UAV flew in the X-Y plane in a boustrophedon pattern and returned to the home point. During the test, two full-cycle trajectory flights were conducted; Fig. 14 shows the actual flight paths, and Fig. 15 presents the actual trajectories of the test UAV.

In both flying tests, the UAV demonstrated suitable trajectory tracking capability, as shown in Fig. 14. The actual path closely matched with the reference trajectory during the straight-line regions of the planned trajectory (such as points 1–2 and 5–6). This indicates that the control system retains excellent accuracy and stability under low dynamic situations. The plots of latitude, longitude and altitude over time in Fig. 16 further demonstrate this; shortly after launch, the UAV reaches and sustains a constant altitude of roughly 6 m (in the range 0–20 s). During phases of rapid turns or attitude changes (e.g., 40–60 s, 100–120 s), deviations from the reference path reach approximately 0.2–0.3 m. Nonetheless, the system typically returns to the reference trajectory in 5–8 s. Overall, the UAV showed stable performance, indicating that the chosen control strategy satisfies the accuracy requirements for repeated agricultural operations, even though there is potential for improvement under high dynamic scenarios.

Fig. 13 Assembly and configuration of a UAV for agricultural plant protection.

Fig. 14 Experimental setup for UAV plant protection trials.

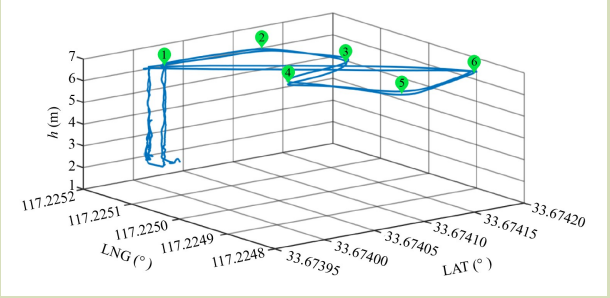

Fig. 15 Actual trajectories of the test UAV.

The system gave outstanding overall control performance, as shown in Fig. 17. Figure 17(a) plots the tracking performance of the roll angle: the command signal and the actual response are nearly in sync, with the greatest error amplitude staying

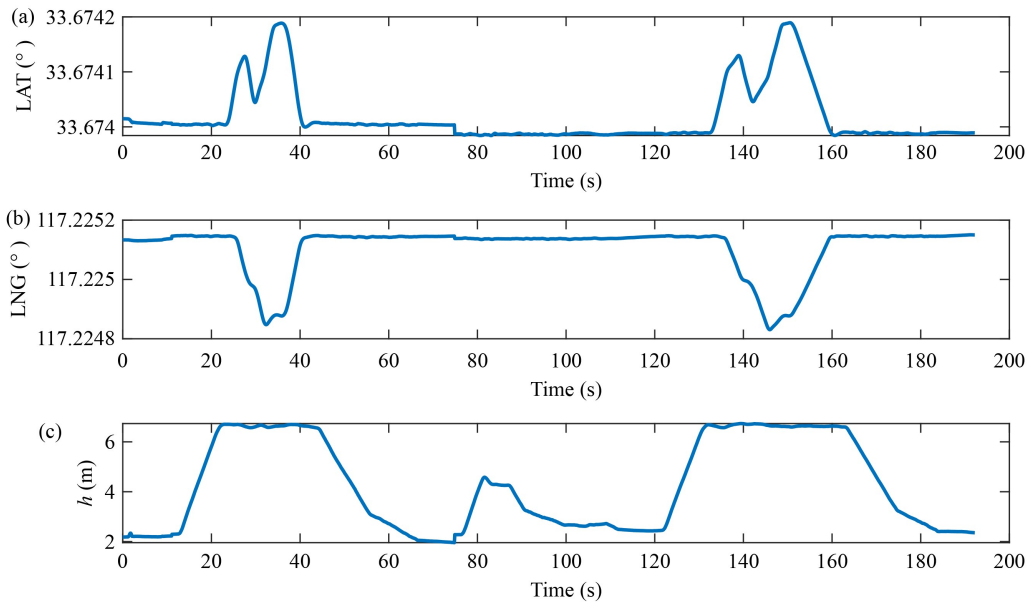

Fig. 16 Experimental results of trajectory tracking: (a) latitude (LAT), (b) longitude (LNG), and (c) height (*h*).

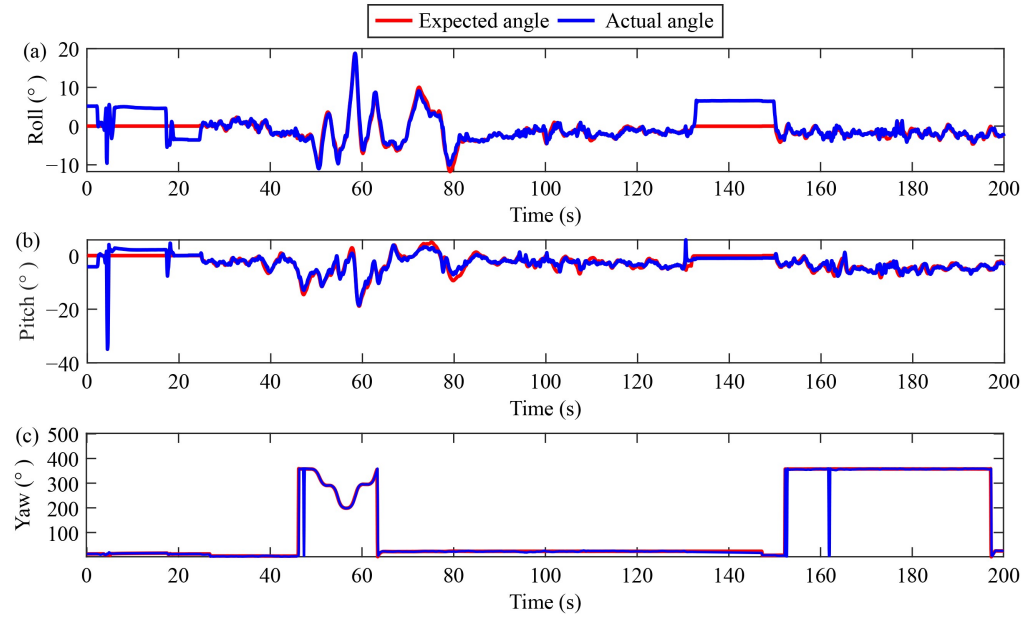

Fig. 17 Experimental results of attitude control: (a) roll angle, (b) pitch angle and (c) yaw angle.

within ±10°; error fluctuations are typically small, and the response quickly adapts to changes in the command signal. Figure 17(b) depicts the pitch angle tracking, which also shows a high degree of consistency, with errors primarily limited to ±5°, demonstrating the robust dynamic adaptation and disturbance rejection ability of the controller. Figure 17(c) presents the yaw angle tracking, which is especially noteworthy: the command signal nearly exactly matches the actual response, and errors stay close to zero for most of the flight; only during abrupt directional shifts do minor deviations happen, and the system promptly corrects them. All things considered, the system accomplishes accurate and dynamically stable attitude control along all three axes, demonstrating the efficacy and resilience of the chosen control algorithm and offering strong experimental backing for more application-focused study.

6 Conclusions

This study addresses the instability and model uncertainty challenges arising from load-induced changes in the dynamics of variable-load quadrotor UAV used in agricultural plant protection tasks. There are three key conclusions. (1) The time-varying dynamic model of the variable-load UAV was constructed as two parts: UAV body model and pesticide tank model. The variation in rotational inertia caused by load changes is considered in the model to reflect the time-varying nature. (2) A PD sliding mode control-based flight control method is proposed to guarantee quick error response and improved performance by creating a nonlinear, time-varying dynamic model and utilizing the complimentary advantages of sliding mode and PD control. (3) The proposed method greatly increases attitude stability and trajectory tracking accuracy with dynamically fluctuating payloads. With small average absolute errors in the *X*-, *Y*- and *Z*-directions. Flight tests validate the method efficacy and illustrate its flight performance. The UAV effectively follows the predetermined course in actual flying testing. It provides valuable technological knowledge for improving automation and intelligence in agricultural plant protection.

Future research will focus on four directions. First, fault-tolerant cooperative control for variable-load UAVs will be developed using distributed observation and adaptive compensation. Second, fault-tolerant containment of UAV swarms will be achieved through sliding mode observation and finite-time consensus. Third, sloshing-induced oscillations will be mitigated by coupled load-fluid modeling and disturbance-rejection control. Fourth, robust algorithms based on disturbance observation and dynamic compensation will be validated through flight experiments in perturbed wind fields.

Acknowledgements

This work was supported by National Natural Science Foundation of China (12402413). The authors also thank the Key Laboratory of Forestry Equipment and Automation, National Forestry and Grassland Administration of China for providing technical support and experimental facilities.

Compliance with ethics guidelines

Xin Zhang, Shuting Xu, Wenjie Chang, and Feng Kang declare that they have no conflicts of interest or financial conflicts to disclose. This article does not contain any studies with human or animal subjects performed by any of the authors.

REFERENCES

1. Lan Y, Yan Y, Wang B, Song C, Wang G. Current status and future development of key technologies for intelligent pesticide spraying robots. *Transactions of the Chinese Society of Agricultural Engineering*, 2022, **38**(20): 30–40 (in Chinese)
2. Zhan Y, Chen P, Xu W, Chen S, Han Y, Lan Y, Wang G. Influence of the downwash airflow distribution characteristics of a plant protection UAV on spray deposit distribution. *Biosystems Engineering*, 2022, **216**: 32–45
3. Zhang Y, Zheng H J, Liu H T, Wei L J, Shen D Z, Zhao Z H. Adaptive RBF neural networks for appointed-time performance control of quadcopter UAVs with model uncertainty. *Transactions of the Chinese Society for Agricultural Machinery*, 2024, **55**(4): 64–73 (in Chinese)
4. Liang X, Liu B, Ye H, Pei T, Yu H, Fang Y. A review of research

on cable-suspended payload transportation systems by rotorcraft unmanned aerial vehicles. *Control and Decision*, 2025, **40**(4): 1079–1097 (in Chinese)

5. Zhang D, Wang S P, Shi M J, Wang D Y, Zhu J X. A disturbance modeling and adaptive control method for autonomous aerial refueling. *Journal of Astronautics*, 2024, **45**(3): 433–442 (in Chinese)
6. Yi K, Gu F, Yang L, He Y, Han J. Sliding Mode Control for a Quadrotor Slung Load System. In: 2017 36th Chinese Control Conference (CCC), Dalian, China. *IEEE*, 2017, 3697–3703
7. Qian L, Liu H H T. Dynamics and Control of a Quadrotor with a Cable Suspended Payload. In: 2017 IEEE 30th Canadian Conference on Electrical and Computer Engineering (CCECE), Windsor, ON, Canada. *IEEE*, 2017, 1–4
8. Tran V P, Santoso F, Garratt M A, Petersen I R. Adaptive second-order strictly negative imaginary controllers based on the interval type-2 fuzzy self-tuning systems for a hovering quadrotor with uncertainties. *IEEE/ASME Transactions on Mechatronics*, 2020, **25**(1): 11–20
9. Pounds P E I, Bersak D R, Dollar A M. Stability of small-scale UAV helicopters and quadrotors with added payload mass under PID control. *Autonomous Robots*, 2012, **33**(1-2): 129–142
10. Xu B. Disturbance observer-based dynamic surface control of transport aircraft with continuous heavy cargo airdrop. *IEEE Transactions on Systems, Man, and Cybernetics. Systems*, 2017, **47**(1): 161–170
11. Cao G Q, Li Y B, Nan F, Liu D, Chen C, Zhang J L. Development and analysis of plant protection UAV flight control system and route planning research. *Transactions of the Chinese Society for Agricultural Machinery*, 2020, **51**(8): 1–16 (in Chinese)
12. Xu J H, Ma H, Zhou J F, Tian Y Q, Han W T. Hovering attitude control of tilt rri-rotor VTOL aircraft. *Transactions of the Chinese Society for Agricultural Machinery*, 2018, **49**(10): 16–22 (in Chinese)
13. Arrieta O, Campos D, Rico-Azagra J, Gil-Martínez M, Rojas J D, Vilanova R. Model-based optimization approach for PID control of pitch–roll UAV orientation. *Mathematics*, 2023, **11**(15): 3390
14. Mateo Sanguino T J, Lozano Domínguez J M, 0. Lozano Domínguez J M. Design and stabilization of a Coandă effect-based UAV: comparative study between fuzzy logic and PID control approaches. *Robotics and Autonomous Systems*, 2024, **175**: 104662
15. Lopez-Sanchez I, Moreno-Valenzuela J. PID control of quadrotor UAVs: a survey. *Annual Reviews in Control*, 2023, **56**: 100900
16. Liu J L, Zhang Z X, Xu T L, Deng H Z. Distributed controller design of UAV swarm under weak path constraints based on adaptive communication topology. *Journal of Astronautics*, 2022, **43**(5): 665–674 (in Chinese)
17. Sir Elkhatem A, Naci Engin S. Robust LQR and LQR-PI control strategies based on adaptive weighting matrix selection for a UAV position and attitude tracking control. *Alexandria Engineering Journal*, 2022, **61**(8): 6275–6292
18. Ahmad F, Kumar P, Bhandari A, Patil P P. Simulation of the quadcopter dynamics with LQR based control. *Materials Today: Proceedings*, 2020, **24**: 326–332
19. Wu H T, Liu J H, You Z R, Wang J L, Wang J H. Multi-model adaptive control of quadrotor UAV hovering. *Automation Application*, 2025, (2): 1–5 (in Chinese)
20. Chebbi J, Briere Y. Robust active disturbance rejection control for systems with internal uncertainties: multirotor UAV application. *Journal of Field Robotics*, 2022, **39**(4): 426–456
21. Song J, Hu Y, Su J, Zhao M, Ai S. Fractional-order linear active disturbance rejection control design and optimization based improved sparrow search algorithm for quadrotor UAV with system uncertainties and external disturbance. *Drones*, 2022, **6**(9): 229
22. Zhou H, Bao X P, Zhang H G. Improved design of phase modulation compensation and analysis of disturbance suppression for UAV active disturbance rejection control. *Acta Armamentarii*, 2024, **45**(10): 3619–3630 (in Chinese)
23. Li S C, Wang F G, Wang S W, Chang T X, Wei Y C. Design and experiment of rotor control system for composite wing unmanned aerial vehicle based on improved ADRC. *Transactions of the Chinese Society for Agricultural Machinery*, 2024, **55**(6): 68–79 (in Chinese)
24. Derrouaoui S H, Bouzid Y, Doula A, Boufroua M A, Belmouhoub A, Guiatni M, Hamissi A. Trajectory tracking control of a morphing UAV using radial basis function artificial neural network based fast terminal sliding mode: theory and experimental. *Aerospace Science and Technology*, 2024, **155**: 109719
25. Li Y F, Wen Y Z, Huang L W. Robust trajectory tracking control of quadrotor UAV based on the improved extended state observer. *Chinese Journal of Scientific Instrument*, 2023, **44**(4): 129–139 (in Chinese)
26. Liang H J, Li J L, Zhu X Y, Zhang Y Y. Trajectory tracking control of a quadrotor UAV based on a fast adaptive super-twisting sliding mode algorithm. *Control Engineering of China*, 2025, [Published Online] doi:10.14107/j.cnki.kzgc.20240269 (in Chinese)
27. Wang Z, Zhao T. Based on robust sliding mode and linear active disturbance rejection control for attitude of quadrotor load UAV. *Nonlinear Dynamics*, 2022, **108**(4): 3485–3503
28. Liu Y, Xing H Y, Hou T H. Research on attitude control of cascade variable universe fuzzy PID for quadrotor UAV. *Journal of Electronic Measurement and Instrumentation*, 2019, **33**(10): 46–52 (in Chinese)
29. Chen G, Song G M, Hao S, Gu Y, Song A G. Modeling and

control of a fully-actuated hexarotor with double-tilted rotors. *Chinese Journal of Scientific Instrument*, 2021, **42**(12): 254–262 (in Chinese)

30. Han J. Auto- disturbances- rejection controller and its application. *Control and Decision*, 1998, **13**(1): 19–23 (in Chinese)
31. Zheng L, Deng F, Yu Z, Luo Y, Zhang Z. Multilayer neural dynamics-based adaptive control of multirotor UAVs for tracking time-varying tasks. *IEEE Transactions on Systems, Man, and Cybernetics. Systems*, 2022, **52**(9): 5889–5900
32. Han Q, Liu Z, Su H, Liu X. Adaptive trajectory tracking control for VTOL UAVs with unknown time-varying mass using an extended I&I estimator. *International Journal of Adaptive Control and Signal Processing*, 2024, **38**(3): 1080–1097
33. Zhou L, Zhang J, Dou J, Wen B. A fuzzy adaptive backstepping control based on mass observer for trajectory tracking of a quadrotor UAV. *International Journal of Adaptive Control and Signal Processing*, 2018, **32**(12): 1675–1693